Lithospheric Structure of the Central Altyn Tagh Fault System Revealed by Teleseismic Travel-Time Tomography

Shi Yao[1,2], Tao Xu[*1,3], Tingwei Yang[1,2], Chenglong Wu[1,3], Jiyan Lin[4], Yujin Hua[5], Dengda Zhu[2,6], and Lingling Ye[7]

Abstract

The Altyn Tagh fault (ATF) system forms the northern margin of the Tibetan Plateau and plays a crucial role in the uplift and development of the Tibetan Plateau. It mediates the far-field effect of the collision between the Indian and the Eurasian plates. Because of limited constraints on the lithospheric velocity structure, the detailed deformation pattern of the central ATF system remains unclear. With a dense seismic array, 483 stations with an interval of ∼1 km, across the central ATF system (the Tarim–Altyn–Qaidam dense nodal array) in late 2021, we obtain 14,079 high-quality teleseismic *P*-wave relative travel-time residuals calculated with the multichannel cross-correlation method, and construct a *P*-wave velocity model beneath the central ATF system via the fast marching tomography (FMTOMO) method. Our results reveal distinct crustal structures in the Western Qaidam basin, Altyn Tagh range, and Eastern Tarim basin. The vertically low *P*-wave velocity anomaly below the ATF, extending down to 130 km, indicates that the ATF is deep fault in the lithospheric scale. The laterally expanded low *P*-wave velocity anomaly beneath the northwest Qaidam from surface to ∼60 km depth indicates the extrusion of Qaidam block, driven by the far-field effects of the Indo-Eurasian collision. The south-dipping significant low *P*-wave velocity anomaly beneath the southeast Tarim at ∼50 to 140 km depth indicates the underthrusting of the Tarim block, providing direct evidence of the clockwise rotation of the Tarim block.

Cite this article as Yao, S., T. Xu, T. Yang, C. Wu, J. Lin, Y. Hua, D. Zhu, and L. Ye (2025). Lithospheric Structure of the Central Altyn Tagh Fault System Revealed by Teleseismic Travel-Time Tomography, *Seismol. Res. Lett.* **96**, 2300–2310, doi: 10.1785/0220240314.

Supplemental Material

Introduction

The Tibetan Plateau, formed by the Indo-Eurasian collision over the past 50 million years, stands at an average elevation of over 4000 m (Yin and Harrison, 2000; Tapponnier *et al.*, 2001). The approximately 1600-km-long east–west-striking Altyn Tagh fault (ATF) system on the northern edge of the plateau delineates the Tarim basin from the Tibetan Plateau (Fig. 1a). This fault system absorbs 10%–25% of the north–south shortening of the entire Tibetan Plateau (Molnar *et al.*, 1987); therefore, it significantly influences the uplift and expansion of the plateau and mediates the far-field effects of the Indo-Eurasian collision (Molnar and Tapponnier, 1975; Shen, Wang, *et al.*, 2001; Tapponnier *et al.*, 2001; Yin *et al.*, 2002; Li *et al.*, 2006; Xu *et al.*, 2011). The ATF has accumulated slip of ∼360 km due to the northward expansion of the Tibetan Plateau with two stages: relatively slow slip from the early Eocene (∼49 Ma) to the Miocene (∼15 Ma), and then fast slip since the late Miocene (Cheng *et al.*, 2015). The geodetic observations indicate that the current slip rate of the western section of the ATF is ∼13 mm/yr, which gradually decreases eastward to be ∼10 mm/yr in the middle section and ∼0.1 mm/yr at the eastern end (Peltzer *et al.*, 1989; Bendick *et al.*, 2000; Wallace *et al.*, 2004; Zhang *et al.*, 2007; He *et al.*, 2013; Li *et al.*, 2018). Isotope and geochronological studies indicate that the deformation along the ATF has been accompanied by the rapid uplift of the Altyn Tagh range (ATR), resulting in more than 2000 m difference in elevation with the Tarim basin (Jolivet *et al.*, 2001; Sobel *et al.*, 2001; Song *et al.*, 2019).

The underthrusting North Altyn Tagh fault (NAF) and the strike-slip ATF separate different geological units from southeast to the northwest across the ATF fault sytem: the Eastern

1. State Key Laboratory of Deep Petroleum Intelligent Exploration and Development, Institute of Geology and Geophysics, Chinese Academy of Sciences, Beijing, China; 2. University of Chinese Academy of Sciences, Beijing, China, https://orcid.org/0009-0004-7933-3357 (DZ); 3. Innovation Academy for Earth Science, Chinese Academy of Sciences, Beijing, China; 4. Geophysical Exploration Center, China Earthquake Administration, Zhengzhou, China; 5. Department of Earth Sciences and Engineering, Taiyuan University of Technology, Taiyuan, China; 6. Key Laboratory of Earth and Planetary Physics, Institute of Geology and Geophysics, Chinese Academy of Sciences, Beijing, China; 7. Department of Earth and Space Sciences, Southern University of Science and Technology, Shenzhen, China, https://orcid.org/0000-0001-9689-4149 (LY)

*Corresponding author: xutao@mail.iggcas.ac.cn

© Seismological Society of America

Downloaded from http://pubs.geoscienceworld.org/ssa/srl/article-pdf/96/4/2300/7126859/srl-2024314.1.pdf
by University of Cambridge user

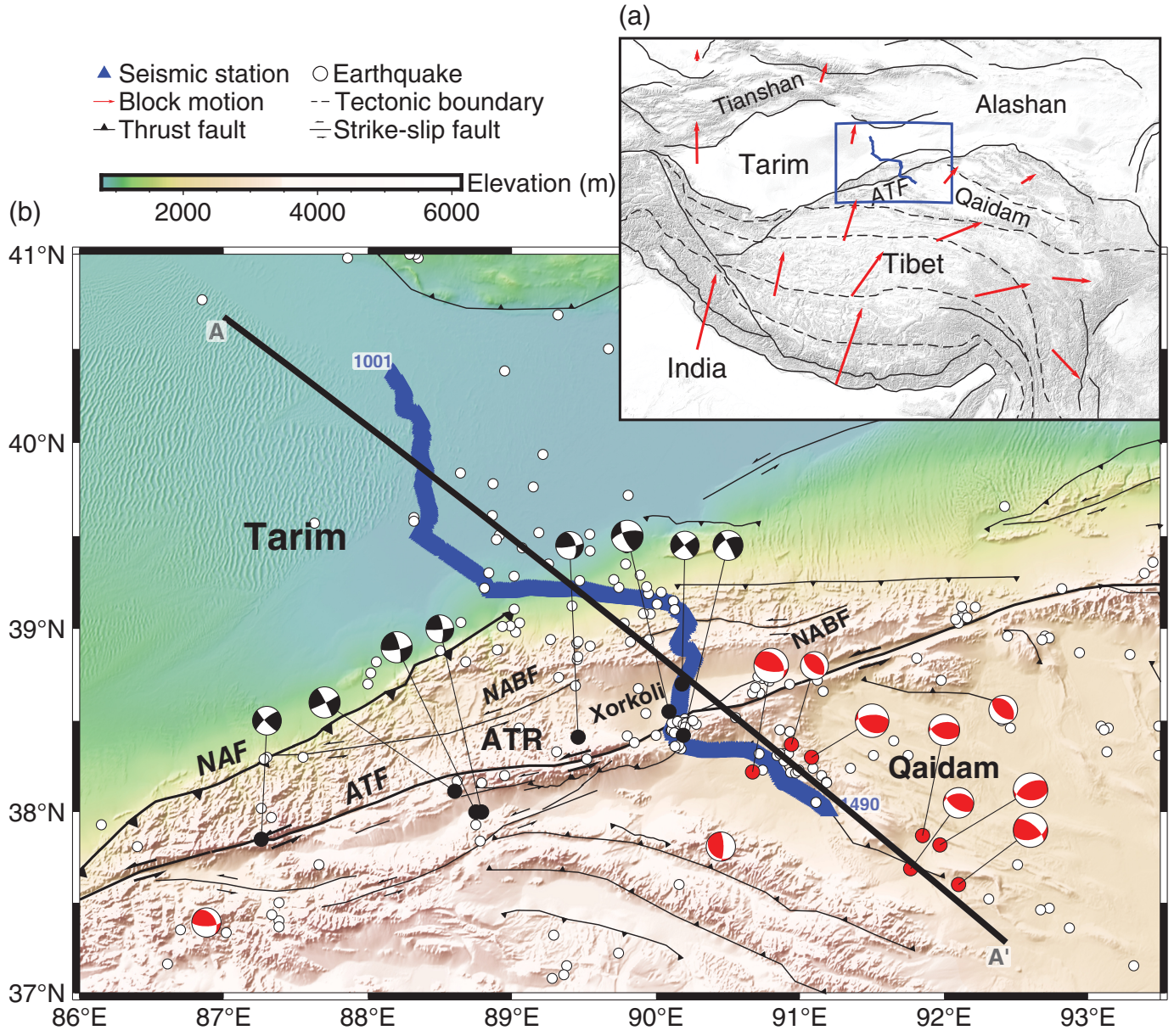

Figure 1. (a) Tectonic setting of the Tibetan Plateau. Solid and dashed black lines indicate main faults and block boundaries (Styron *et al.*, 2010, see Data and Resources). The red arrows show the average GPS velocity field (Wang and Shen, 2020). (b) Tectonic setting of the central Altyn Tagh Fault system and location of the dense nodal array (blue triangles). White dots show earthquakes during the deployment of the array (Yao *et al.*, 2024) and $M_L > 3$ events from the International Earthquake Science Data Center (see Data and Resources) from 2007 to 2022. Focal mechanisms are from the Global Centroid Moment Tensor catalog (Global CMT, see Data and Resources), with strike-slip and thrusting earthquakes filled in black and red, respectively. AA′ marks the tomography profile along our dense array. ATR, Altyn Tagh Ragne; ATF, Altyn Tagh fault; NAF, North Altyn Tagh fault; NABF: North Altyn Branch fault.

Tarim basin (ETB), the ATR, and the Western Qaidam basin (WQB; Fig. 1b). Tarim and Qaidam basins have significantly different elevations but are both widely covered by sediments (Sobel, 1999; Xia *et al.*, 2001; Shen *et al.*, 2022). In contrast, the ATR mainly consists of bedrock except for a small strike-slip basin, Xorkoli basin, covered by Cenozoic sediments (Mann *et al.*, 1983; Christie-Blick and Biddle, 1985; Guo *et al.*, 1998). The difference in elevation and sedimentary coverage is associated with active slip and uplift activities along the ATR (Yin *et al.*, 2002; Chen *et al.*, 2003). The low seismicity within Qaidam basin, Tarim basin, and ATR indicates that the ETB remains relatively stable, whereas the seismic activity is concentrated primarily along the ATF and the associated secondary thrust faults to its south (Fig. 1; Yao *et al.*, 2024). Most earthquakes along the ATF are predominantly strike slip, whereas those along the secondary thrust faults to the south are primarily thrust earthquakes, suggesting complex deformation patterns. Thus, it is crucial to image the detailed deep structure of the ATF system to elucidate its regulatory role in the far-field effects of the Indo-Eurasian collision to further

Downloaded from http://pubs.geoscienceworld.org/ssa/srl/article-pdf/96/4/2300/7126859/srl-2024314.1.pdf
by University of Cambridge user

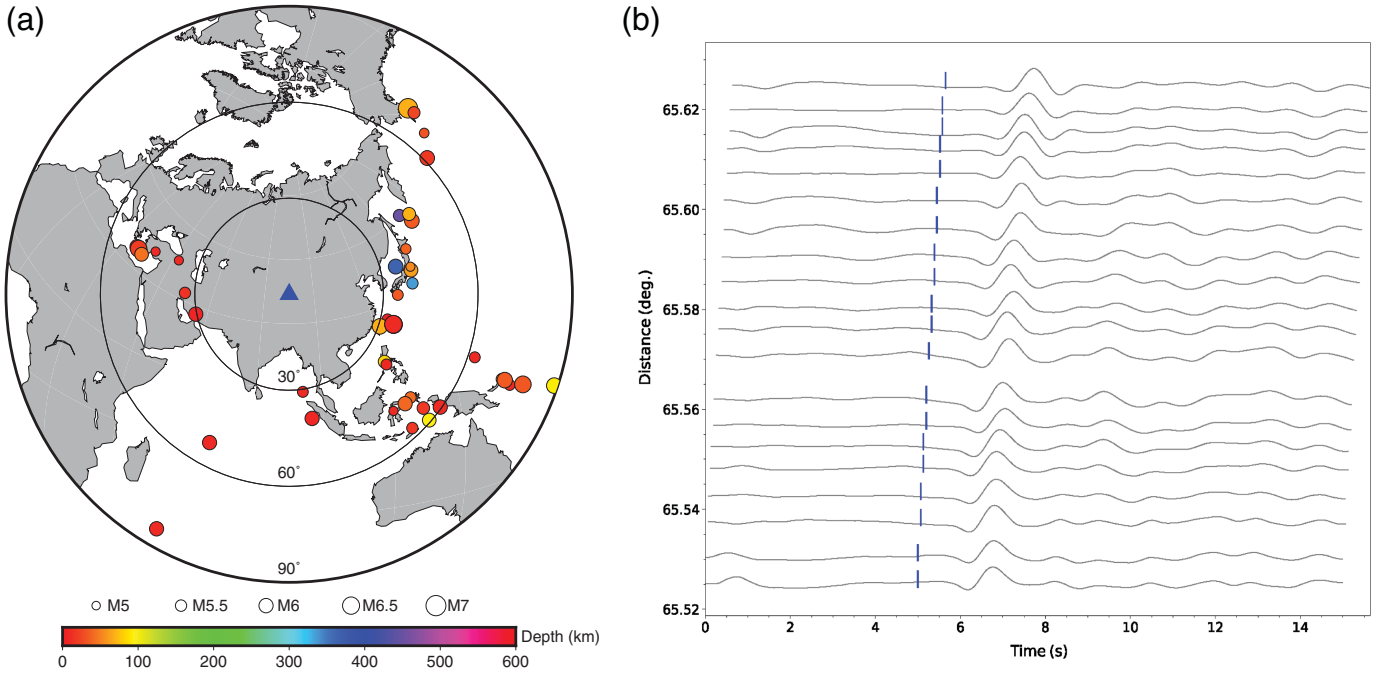

Figure 2. Data used in this study. (a) The locations of 45 teleseismic events are from the U.S. Geological Survey National Earthquake Information Center (USGS-NEIC) catalog (see Data and Resources), color coded by their source depths. Blue triangles indicate the dense nodal array. (b) Sample waveforms of vertical components (event: 1 October 2021_00:10:52.386, M_b 5.2). Blue-solid bars mark the predicted *P* arrivals.

understand the mechanisms behind the uplift and extension of the Tibetan Plateau.

Geophysical observations, in the central ATF system, suggest that the Tarim lithosphere underthrusts beneath the ATR (Zhao *et al.*, 2006; Shi *et al.*, 2007; Zhang *et al.*, 2015) with some implication of the ATF's extension scale (Wittlinger *et al.*, 1998; Herquel *et al.*, 1999; Shi *et al.*, 1999; Jiang *et al.*, 2004). The gravity survey shows that the ATF is nearly vertical and cuts through the entire lithosphere (Jiang *et al.*, 2004). Wittlinger *et al.* (1998) identified a low-velocity anomaly extending to about 140 km below the ATF from teleseismic tomography image and concluded that the ATF is not confined to the crust but also controls the extrusion of large blocks on a lithospheric scale such as the Tibetan Plateau and the Qaidam basin. The vertical-coherent deformation from the teleseismic shear-wave splitting analysis also supports the view that the ATF cuts through the crust (Herquel *et al.* 1999). However, Zhao *et al.* (2006) interpreted a flat Moho interface below the ATF from artificial source seismic refraction and wide-angle reflection, which suggests that the ATF is an intracrustal fault.

In this study, we plan to use the Tarim–Altyn–Qaidam dense nodal array data we deployed in late 2021 to obtain the lithospheric velocity structure of the central ATF system with the fast marching tomography (FMTOMO) method using the teleseismic travel-time observation. With the tomography image, we can discriminate the deep deformation patterns from the WQB to the ETB across the central ATF system in the northern margin of the Tibet Plateau and illustrate the relationship with the Indo-Eurasian collision.

Data and Method

We used the data from the Tarim–Altyn–Qaidam dense nodal array deployed from 17 September to 23 November 2021. The array consists of 483 seismic stations with station intervals of ~1 km, resulting in a profile of ~430 km across the central ATF system (Xie *et al.*, 2023, 2024; Wu *et al.*, 2024). Each station is equipped with three-component EPS-5S and EPS-20S seismometers, sampling at 100 Hz. In this study, we use 477 seismic stations, excluding six seismometers due to clock drift (Yao *et al.*, 2024).

We select earthquakes with epicentral distances between 30° and 90° and $m_b > 5$ during deployment. The teleseismic waveform data are preprocessed by removing the mean, tilt, and instrument response, and band-pass filtered within a 0.1–1 Hz range. We use a multichannel cross-correlation method (VanDecar and Crosson, 1990; Wang *et al.*, 2019) to extract the teleseismic relative travel-time residuals (see details in Text S1, available in the supplemental material to this article). We kept residuals with uncertainty no more than 0.2 s, cross-correlation coefficient > 0.75 and more than 100 records for one event. We retain 14,079 *P*-wave relative travel-time residuals from 45 teleseismic earthquakes, and ray paths cover areas of east, south, and these events are predominantly located in the Pacific Rim seismic belt, covering areas to the east, south, and west of the array with limited data from the north (Fig. 2).

We utilize the fast marching method (FMM, see Data and Resources) to calculate the velocity sensitivity kernels for both teleseismic and local ray paths (de Kool *et al.*, 2006) and assess

Downloaded from http://pubs.geoscienceworld.org/ssa/srl/article-pdf/96/4/2300/7126859/srl-2024314.1.pdf
by University of Cambridge user

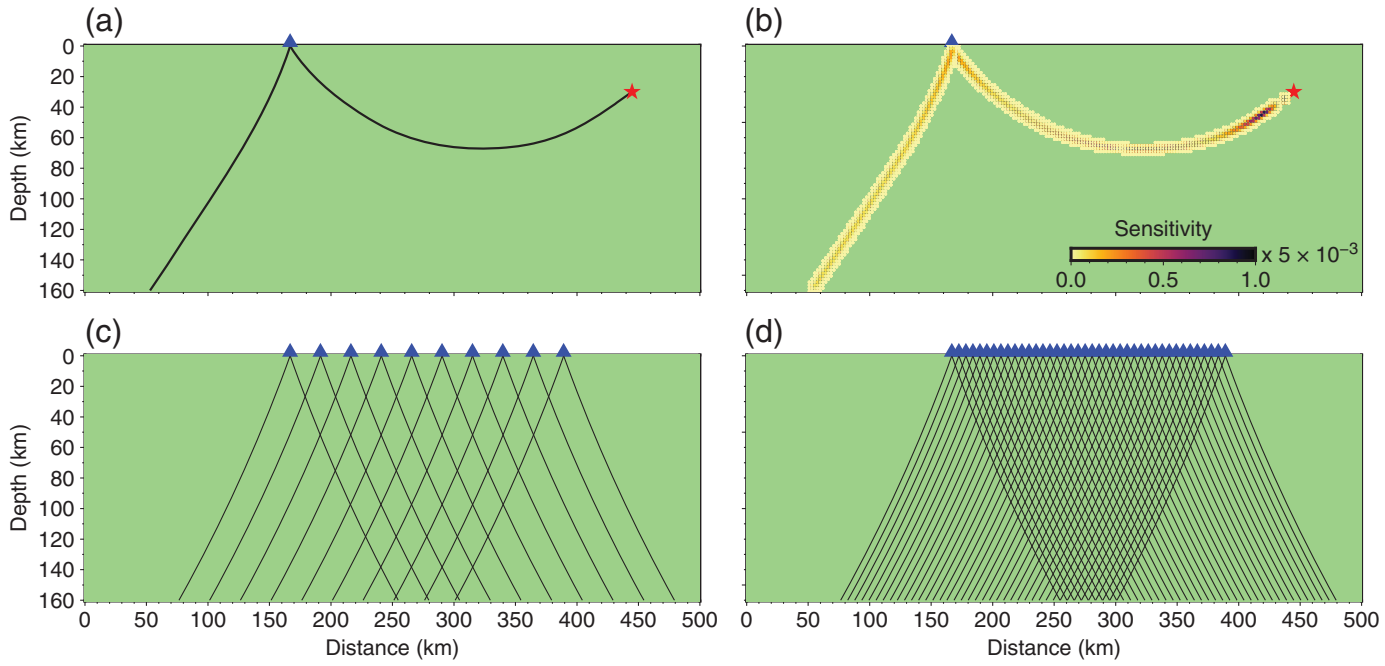

Figure 3. (a) Comparison of teleseismic and local seismic ray paths with red star and blue triangle indicating the earthquake source and station, respectively. (b) The corresponding sensitivity kernels. (c) Coverage of teleseismic rays with a station interval of 20 km. (d) Coverage of teleseismic rays with a station interval of 5 km.

the teleseismic ray coverages at different station intervals based on synthetic data tests (Fig. 3). Teleseismic rays, equivalent to local seismic rays with the source located at the bottom interface, exhibit sensitivity to model parameters similar to that of local rays (Fig. 3b). With a 20 km interval, the teleseismic rays intersect below a depth of 30 km (Fig. 3c), whereas with a 5 km interval, ray intersections are observed at depths above 10 km (Fig. 3d). When stations are densely spaced, teleseismic observations can be effectively utilized to obtain the velocity structure of the shallow crust. In this study, with station interval of ~1 km, rays are intersected even at depths of 1–2 km.

We employ the FMTOMO method (de Kool *et al.*, 2006) for teleseismic tomography. The FMTOMO uses the FMM to calculate travel times and applies subspace inversion to solve the linearized inversion problem. FMM is a grid-based Eikonal equation solver (Sethian, 1996), which uses a narrow band method to track wavefronts and an upwind difference format to numerically solve the Eikonal equation. It can calculate travel times for any source in 3D space (Rawlinson and Sambridge, 2004; Rawlinson, Kool, and Sambridge, 2006). We first use the AK135 model (Kennett *et al.*, 1995) to compute the travel time from the earthquake to the bottom interface of the model. Next, we treat the penetration point at the bottom interface as a new source and calculate the travel time from this point to the seismic station with the FMM using the local velocity model from Zhao *et al.* (2006). For the detailed velocity model, see Table S1 and Figure S1. The objective function of teleseismic tomography for a given model $\mathbf{m}$ is given by (Rawlinson, Reading, and Kennett, 2006)

$$S(\mathbf{m}) = (\mathbf{g}(\mathbf{m}) - \mathbf{d}_{\text{obs}})^T \mathbf{C}_d^{-1} (\mathbf{g}(\mathbf{m}) - \mathbf{d}_{\text{obs}}) + \epsilon(\mathbf{m} - \mathbf{m}_0)^T \mathbf{C}_m^{-1} (\mathbf{m} - \mathbf{m}_0) + \eta \mathbf{m}^T \mathbf{D}^T \mathbf{D} \mathbf{m}, \quad (1)$$

in which $\mathbf{g}(\mathbf{m})$ and $\mathbf{d}_{\text{obs}}$ denotes the theoretical and observed relative travel-time residuals, respectively, $\mathbf{m}_0$ is the reference model, $\mathbf{C}_{\text{d}}$ and $\mathbf{C}_m$ are priori data and model covariance, ϵ, η, and $\mathbf{D}$ are damping factor, smoothing factor, and second derivate smoothing operator. For the ith iteration, the model is updated by the model perturbation $\delta\mathbf{m}(\mathbf{m}_{\text{i+1}} = \mathbf{m}_{\text{i}} + \delta\mathbf{m})$, and the subspace inversion technique is used to calculate $\delta\mathbf{m}$ (Kennett *et al.*, 1988).

The stations of the array are placed along roads due to challenging natural conditions, rather than in a straight line, so we choose the tomography section along AA′ in Figure 1b. For teleseismic tomography, all seismic rays must penetrate from the model's bottom interface, and reliable tomography extends to approximately one-third of the array's length (Xu *et al.*, 2009; Schmedes *et al.*, 2012; Tian *et al.*, 2020). Considering the station elevation at about 4 km above the sea level, we define the model space with: longitude from 87° to 93° E, latitude from 36.5° to 41.5° N, and depth from −4 to 160 km, with a grid interval of 0.2° × 0.2° × 16 km.

Results

To evaluate the resolution of observed data along section AA′, we conduct recovery tests of velocity anomalies at various sizes using FMTOMO. In these tests, we incorporate alternating positive and negative velocity anomalies less than ± 3% with ray paths used in actual inversion. In addition, random noise

Downloaded from http://pubs.geoscienceworld.org/ssa/srl/article-pdf/96/4/2300/7126859/srl-2024314.1.pdf
by University of Cambridge user

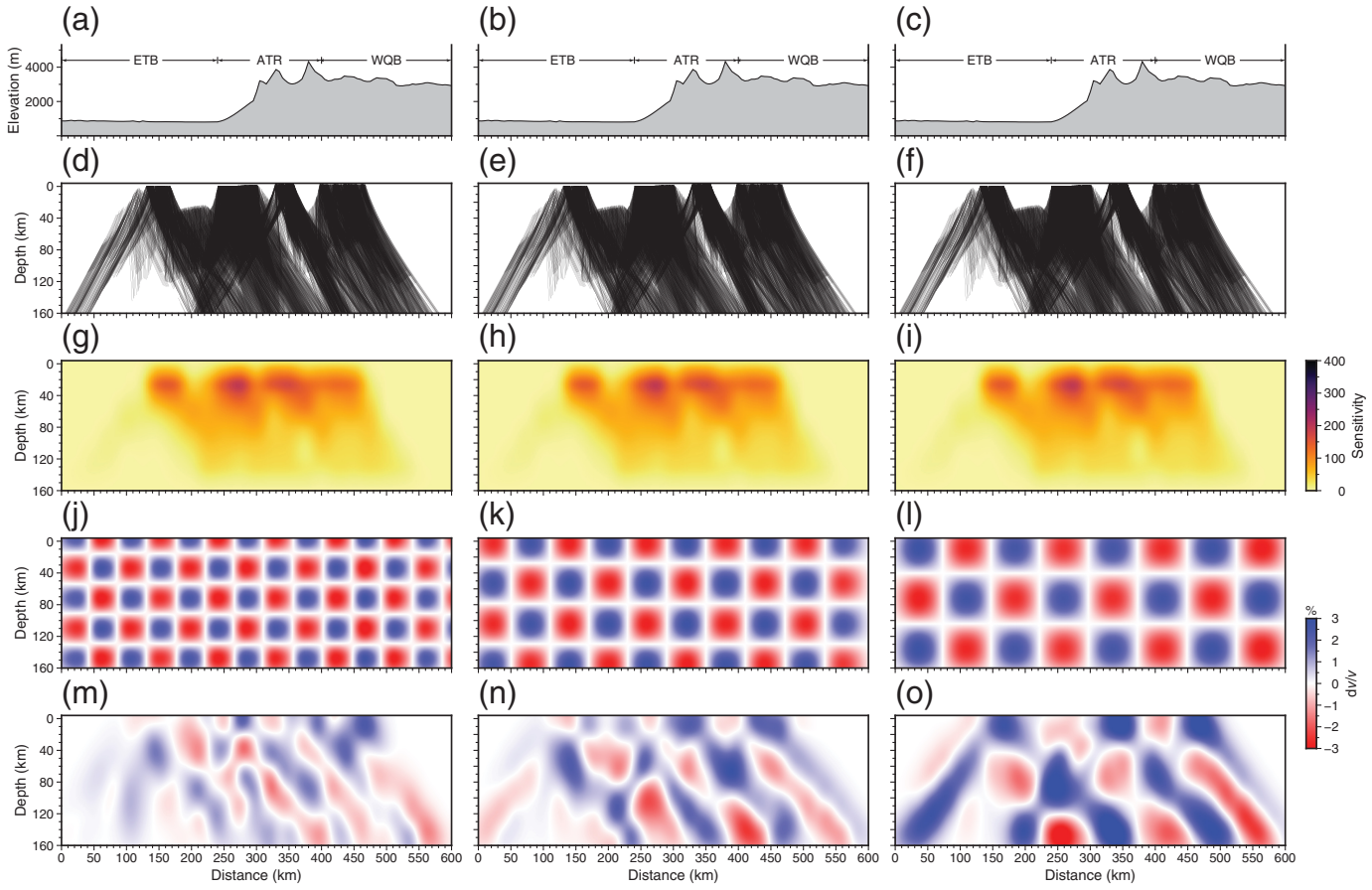

Figure 4. Checkerboard tests of teleseismic tomography with different anomaly sizes. (a–c) Topography along the AA′ profile. (d–f) Rays coverage within 20 km from AA′. (g–i) Sensitivity kernel. Panels (a,d,g), (b,e,h), and (c,f,i) are the same. (j–l) Input checkerboard velocity anomaly (±3%) with different grid sizes. (m–o) Recovered velocity anomaly models.

with a zero mean and a standard deviation of 0.05 s is added to the theoretical travel times to account for errors in our real data set. The sizes of the velocity anomalies were set to 0.3° × 0.3° × 30, 0.4° × 0.4° × 40, and 0.5° × 0.5° × 50 km.

Figure 4 presents the results of the recovery test for teleseismic tomography using checkerboard velocity models of varying anomaly sizes. The dense seismic stations allow for more ray intersections within the crust (Fig. 4d–f), enabling a good resolution for crustal structure (Fig. 4m–o). Because of the nonlinear station arrangement, some stations are located more than 20 km away from the survey line, resulting in areas of the profile with insufficient ray coverage (Fig. 4d–f). As the teleseismic rays are nearly vertically incident, it is challenging to discern whether they intersect or run parallel from ray paths. The sensitivity kernels (Fig. 4g–i) indicate that despite the dense ray coverage, the resolution remains low from 140 to 160 km depth because most rays in this depth range are parallel or nearly parallel with few intersections. Based on the resolution tests, we have a relatively good recovery at distance of about 100–500 km and depth of no more than 140 km (Fig. 4m–o), consistent with the sensitivity results. Future sections will focus on these areas.

To achieve stable convergence and reasonable inversion results, we selected the optimal damping and smoothing factors based on the trade-off between data variance and model variance, data variance and model roughness. When the damping factor is set to 2000, we find an optimal balance between data variance and model variance (Fig. 5a). With the damping factor fixed at 2000, we then determined the optimal smoothing factor by evaluating the trade-off between data variance and model roughness (Fig. 5b). The final smoothing factor was set at 1000, ensuring a moderate velocity anomaly. Figure 6 presents a histogram showing the misfit distribution of the teleseismic relative travel-time residuals before and after inversion. The misfit is significantly reduced and exhibits as gauss distribution.

Benefiting from the strong energy of natural earthquakes and the narrow interval of the dense nodal array, the velocity model obtained in this study has a deeper range than the crustal velocity model of Zhao *et al.* (2006) and a higher resolution than the lithospheric velocity model of Wittlinger *et al.* (1998). The teleseismic rays are nearly vertically incident, and

Downloaded from http://pubs.geoscienceworld.org/ssa/srl/article-pdf/96/4/2300/7126859/srl-2024314.1.pdf
by University of Cambridge user

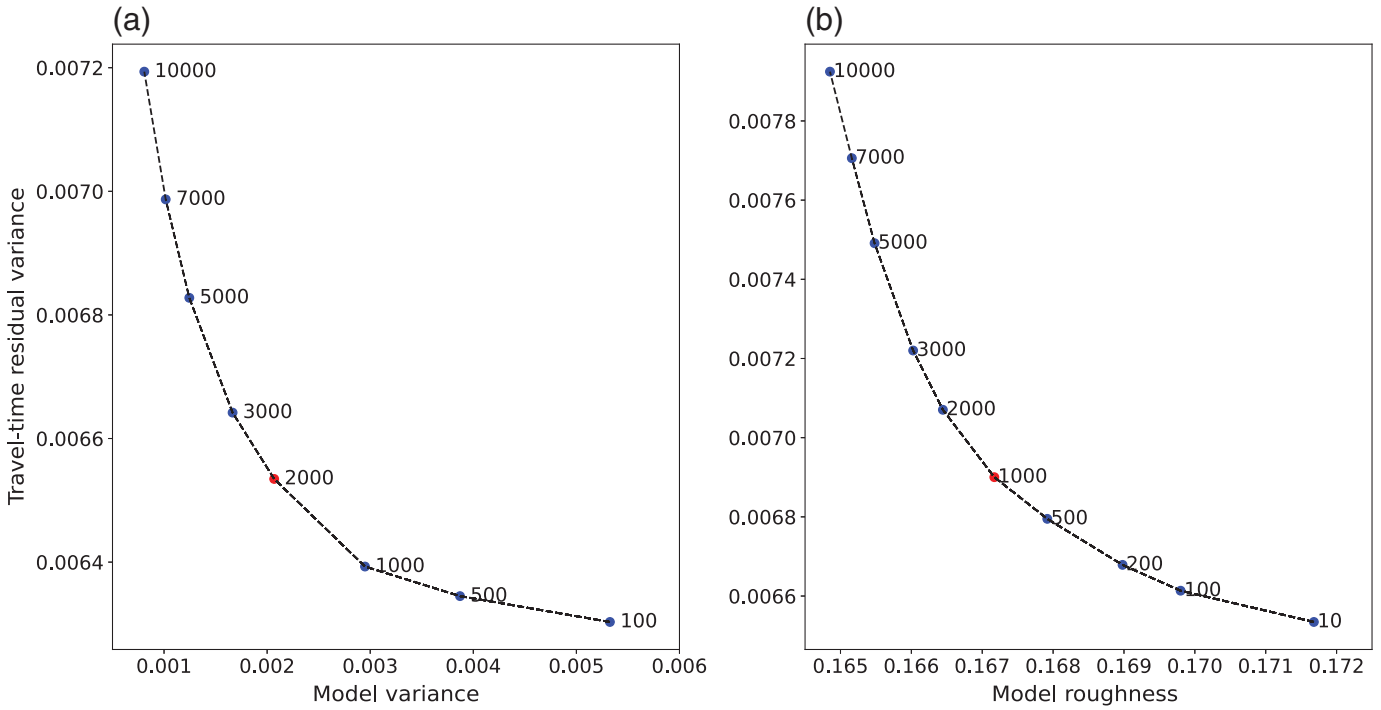

Figure 5. (a) Trade-off curve of data and model variance. The best-damping factor for the inversion is 2000 (red dot). (b) Trade-off curve of data variance and model roughness. The best-smoothing factor for the inversion is 1000 (red dot).

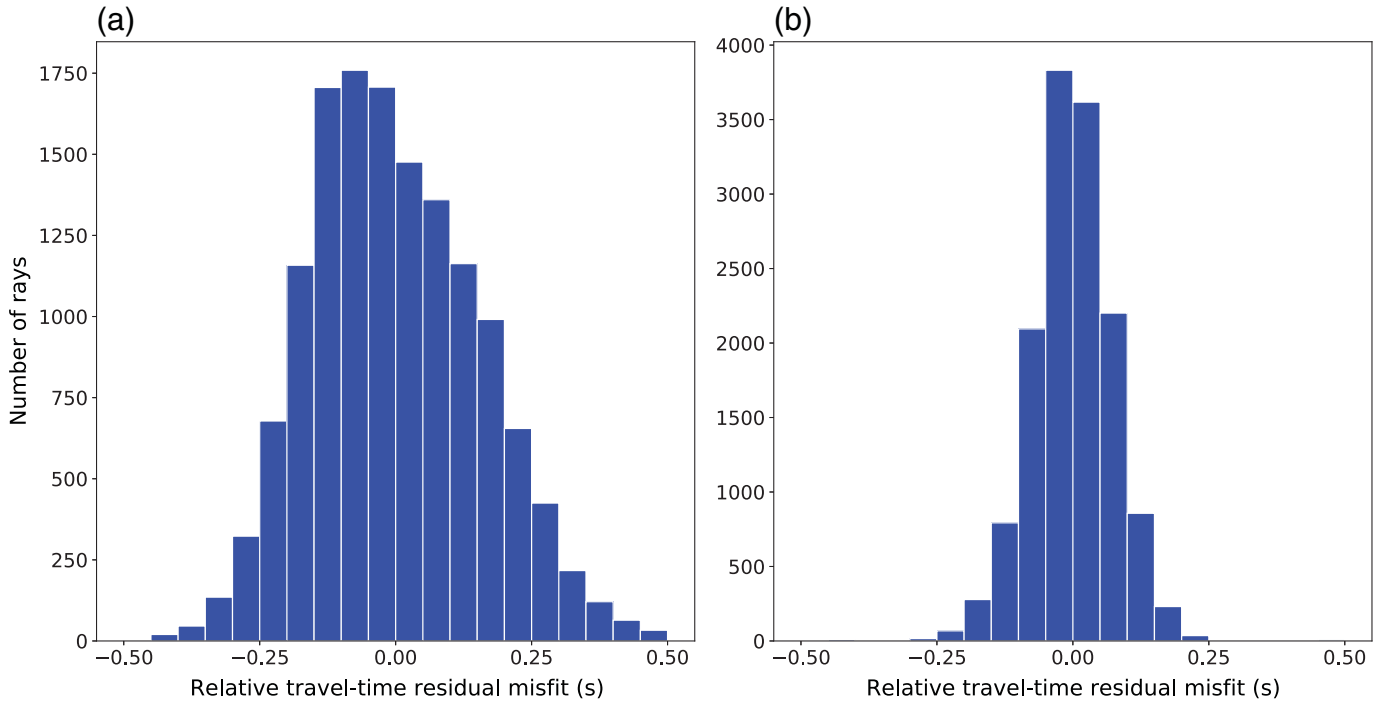

Figure 6. (a) Misfit distribution of relative travel-time residuals with the initial model. (b) Misfit distribution of relative travel-time residuals with our inverted model (Fig. 7).

Downloaded from http://pubs.geoscienceworld.org/ssa/srl/article-pdf/96/4/2300/7126859/srl-2024314.1.pdf
by University of Cambridge user

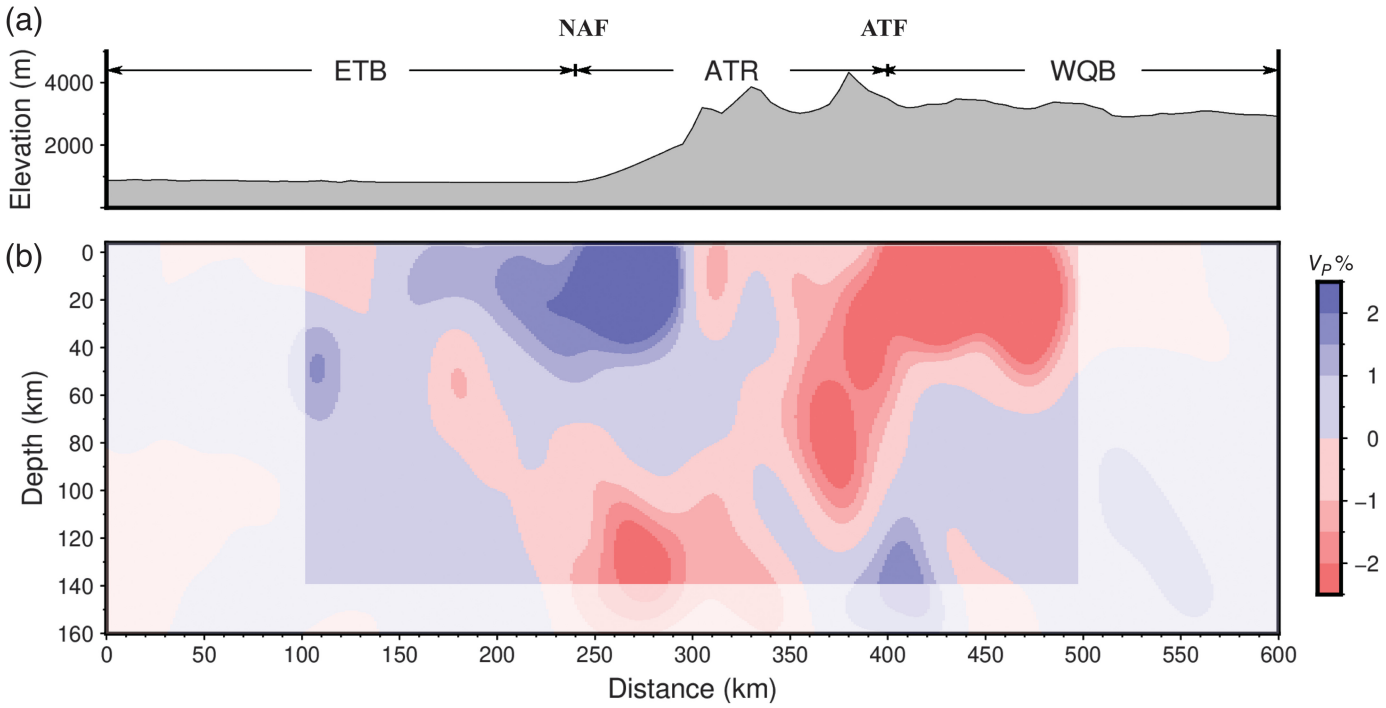

Figure 7. (a) Topographic of the profile AA′. (b) The inverted *P* velocity anomaly with results of teleseismic tomography. The region from about 100–500 km, as highlighted, has relatively high resolution based on our tests in Figure 4. ETB, Eastern Tarim basin; WQB, Western Qaidam basin.

teleseismic relative travel-time residuals are used in the inversion instead of the travel time, which reduces sensitivity to vertical velocity changes and leads to poor vertical resolution (Rawlinson, Reading, and Kennett, 2006; Schmedes *et al.*, 2012). This results in some anomalies appearing "stretched" vertically, a phenomenon also observed in the resolution test (Fig. 4m–o). The lateral resolution of the tomography generally correlates with the station interval. Given that the station interval in this study is about 1 km, the tomography results exhibit high lateral resolution.

In the crust, the ETB, ATR, and WQB show low-velocity anomaly, high-velocity anomaly, and low-velocity anomaly, respectively (Fig. 7). The lateral variation of crustal velocity is consistent with the model from Zhao *et al.* (2006) using the seismic refraction and wide-angle reflection method. The upper crust of part of the ETB and the southeastern part of the ATR lacks ray coverage (Fig. 4d–f), causing the inversion results to be affected by adjacent areas and resulting in significant smearing. These two most significant features in the tomography result are the low-velocity anomaly extending to ∼130 km below the ATF and the low-velocity anomaly extending from beneath the ETB to beneath the ATR. These main features are consistent with the teleseismic tomography results of Wittlinger *et al.* (1998).

Discussions

Crustal structures in the central ATF system

Our tomography image shows a high *P*-wave anomaly in the upper crust in the northwestern part of the ATR (Fig. 8), attributed to its active uplift, which has exposed a substantial amount of bedrock, primarily composed of Cambrian igneous rocks, metamorphic rocks, and Paleozoic sedimentary rocks (Wang, 1997; Sobel *et al.*, 2001). In the ATR, the north Altyn Branch fault is developed, and along with the Xorkoli basin, both have a generally lower *P*-wave velocity compared to the northern ridge area (Fig. 8). Both the ETB and the WQB are covered by Cenozoic sediments, leading to a low *P*-wave velocity anomaly in the upper crust, as observed (Fig. 8).

In the low crust beneath east Tarim basin, the high *P*-wave velocity anomaly (Fig. 8), along with high density (Deng *et al.*, 2017), high resistivity (Zhang *et al.*, 2015), and high-V_P/V_S ratios (Wu *et al.*, 2024), suggests that it may be predominantly composed of mafic components. During the Early Permian, upwelling mantle plumes triggered igneous activity in the Tarim basin and formed a widespread mafic large igneous province (Chen, Yang, *et al.*, 2006; Xu *et al.*, 2014). Aeromagnetic findings indicate that much of the Tarim basin has undergone thermal pulses associated with mantle activity (Xu *et al.*, 2021). The intrusion of ferromagnetic materials has reinforced the Tarim lithosphere, leading to a high *P*-wave-velocity anomaly in the lower crust.

In contrast, the Qaidam basin, situated within the Tibetan Plateau, has a low *P*-wave velocity anomaly in the lower crust (Fig. 8). Compared to the Tarim basin, the Qaidam basin has a thicker crust (Zhao *et al.*, 2006; Wu *et al.*, 2024). The low density (Deng *et al.*, 2017), low-V_P/V_S ratio (Wu *et al.*, 2024), and low-resistance body in the lower crust (Zhang *et al.*, 2015),

Downloaded from http://pubs.geoscienceworld.org/ssa/srl/article-pdf/96/4/2300/7126859/srl-2024314.1.pdf
by University of Cambridge user

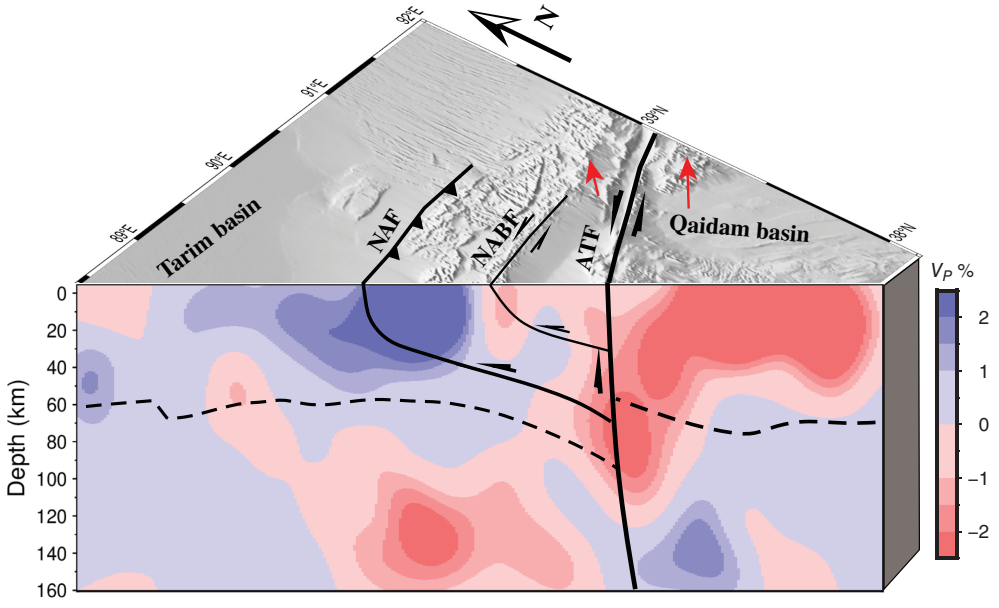

Figure 8. The 3D illustration of lithospheric structure in the central ATF system with our *P* velocity anomaly. The dotted line and the red arrows show the Moho interface (Wu *et al.*, 2024) and GPS velocity measurements (Li *et al.*, 2018), respectively.

suggest that the Qaidam basin has a ductile middle and lower crust, weaker than Tarim basin's crust (Li *et al.*, 2014; Zhou *et al.*, 2023). This observation aligns with the continuous deformation model of the Tibetan Plateau proposed by previous researchers (England and McKenzie, 1982; Shen, Royden, and Burchfiel, 2001), which posits that the Qaidam basin accommodates the north–south contraction of the Tibetan Plateau through crustal shortening and thickening.

ATF: a lithospheric-scale fault

The tomography image shows a low *P*-wave velocity anomaly extending down to about 130 km below the ATF (Fig. 8), indicating that it is a lithospheric-scale fault. It aligns with previous teleseismic tomography results (Wittlinger *et al.*, 1998). Using the same data, Wu *et al.* (2024) found a significant Moho offset of nearly 30 km on either side of the ATF based on the receiver function method. Herquel *et al.* (1999) found that the *SKS* fast wave direction aligns with the fault strike, indicating that the shearing action affects the mantle and it supports that the ATF is a lithospheric-scale fault rather than a crustal-scale fault (Zhao *et al.*, 2006). Magnetotelluric result by Zhang *et al.* (2015) also shows a low-resistance body beneath the ATF, similar to the shape of the low *P*-wave velocity anomaly in our tomography image. The low *P*-wave velocity anomaly could be generated by the mixing of mafic and ultramafic rocks (Zhao *et al.*, 2006), and it would not produce a major change in resistivity as observed in Zhang *et al.* (2015). This low *P*-wave-velocity anomaly indicates the fault zone of ATF has increased porosity and fluid content, acting as a conduit for the upward migration of fluids from deep fluid-rich sources.

Deformation mechanism of the central ATF system

Our tomography image shows a significant south-trending low *P*-wave-velocity anomaly beneath the southeastern margin of Tarim (Fig. 8). This suggests that the Tarim lithosphere may be underthrusting southward beneath the ATR (Wittlinger *et al.*, 1998; Gao *et al.*, 2001; Wang *et al.*, 2024; Wu *et al.*, 2024). Compared with the Central ATF, at the western end of the ATF, the intersection and deformation of the Tarim lithosphere and the lithosphere of the West Kunlun on the northwest edge of the Tibetan Plateau form a "V"-shaped coupling relationship. This configuration aligns more with a model of lithospheric collision rather than the subduction or underthrusting of one plate beneath another (Gao *et al.*, 2001; Kao *et al.*, 2001; Feng *et al.*, 2016). At the western end of the ATF, the rigid Indian plate collides with the Tarim lithosphere. It appears that different segments of the ATF have undergone distinctly varied deformation processes.

The south-dipping low *P*-wave-velocity anomaly beneath the southeastern edge of Tarim indicates a southward motion. Previous seismological studies have shown that at the forefront of the India-Eurasia collision, the Indian lithosphere subducted northward beneath the southwestern margin of the Tibetan Plateau and has reached the Tarim in the West Kunlun region (Rai *et al.*, 2006; Li *et al.*, 2008; Zhao *et al.*, 2010). Geochemical observations in the southeastern Pamir revealed that the Indian slab collided with the Tarim block ~11 Ma in the late Miocene (Shaffer *et al.*, 2017). Concurrently, an upper-mantle low *S*-wave anomaly beneath the southern Tianshan suggests that the Tarim craton underthrusted beneath the southern Tianshan (Li *et al.*, 2022), adding to the Tianshan orogen on the northwest edge of the Tarim basin with uplift and crustal shortening around 10 Ma (Jia *et al.*, 2020; Li *et al.*, 2022). Similarly, our result shows that the Tarim lithosphere underthrusted beneath the ATR, supporting that the ATR on the southeastern edge of Tarim began to uplift around 10 Ma (Chen, Gong, and Li, 2006; Song *et al.*, 2019), with significant crustal shortening starting around 9 Ma (Wu *et al.*, 2024). These phenomena are consistent with the view that the Tarim block underwent clockwise rotation (Chen *et al.*, 1992; Zhao *et al.*, 2019; Cui *et al.*, 2024). Thus, we suspect that the low *P*-wave velocity below the southeastern margin of

Downloaded from http://pubs.geoscienceworld.org/ssa/srl/article-pdf/96/4/2300/7126859/srl-2024314.1.pdf
by University of Cambridge user

Tarim indicates the southward underthrusting of the lithosphere at this margin (Fig. 8), driven by the clockwise rotation of the Tarim block.

The low *P*-wave velocity anomaly beneath the northwest margin of the Qaidam (Fig. 8) is also evident in the tomography model of Wittlinger *et al.* (1998) and Zhao *et al.* (2006). Combining these observations with the shear-wave splitting results, which transition from the west-northwest–east-southeast direction of the Qaidam to the northeast–southwest direction of the ATR (Herquel *et al.*, 1999; Chang and Wang, 2023), and the focal mechanism indicating a shift from thrust to strike slip (Yao *et al.*, 2024), we infer that the low *P*-wave-velocity anomaly reflects the extrusion of the Qaidam block along the ATF in the northeast direction. This extrusion is driven by the far-field effect of the Indo-Eurasian collision, transmitting driving force through the Tibetan Plateau. Consequently, the oblique convergence of the Tarim and Qaidam causes compressional deformation beneath the ATR, with the Tarim lithosphere being squeezed beneath the ATR to prompt the uplift along the ATR.

Conclusions

Based on the dense nodal array data, we obtain the lithospheric velocity structure at the central ATF system with the teleseismic *P*-wave travel-time tomography. We find significantly different crustal velocity structures with a rigid lower crust beneath the Tarim, a relatively weak crust beneath the Qaidam, and active compression and uplift activities in the Altyn Tagh crust. The low-velocity anomaly below the ATF extends to ~130 km on a lithospheric scale. There are two significant low *P*-velocity zones beneath the southeastern margin of Tarim and the northwest margin of Qaidam, revealing the underthrusting of the Tarim lithosphere and the extrusion of the Qaidam lithosphere, associated with the clockwise rotation of the Tarim block and far-field effects of the Indo-Eurasian collision, respectively.

Data and Resources

The International Earthquake Science Data Center searched using http://www.esdc.ac.cn/. The Global Centroid Moment Tensor Project (Global CMT) database was searched using https://www.globalcmt.org/CMTsearch. The National Earthquake Information Center at (NEIC) U.S. Geological Survey (USGS) is available at https://earthquake.usgs.gov/earthquakes/search/. The open-source database of HimaTibet Map was searched using https://github.com/HimaTibetMap/HimaTibetMap. The software fast marching tomography (FMTOMO) was obtained from https://rses.anu.edu.au/~nick/fmtomo.html. All websites were last accessed in August 2024. The supplemental material for this article includes "Text S1: detailed description for extracting teleseismic relative travel-time residuals," "Table S1: detailed initial velocity model for tomography," and "Figure S1: picture of initial velocity model."

Declaration of Competing Interests

The authors acknowledge that there are no conflicts of interest recorded.

Acknowledgments

The authors would like to thank Editor-in-Chief Allison Bent and two anonymous reviewers for their constructive comments. The authors would like to express their sincere gratitude to the Geophysical Exploration Center of China Earthquake Administration for their dedicated efforts in field data collection. Special thanks to Zhiyong Yan, Tongtong Xie, Xiaoyue Wu, and Jinzhi Ma for providing valuable comments and insights that greatly contributed to this study. This study was supported by the Second Tibetan Plateau Scientific Expedition and Research Program (STEP, 2019QZKK0701-02) and the National Natural Science Foundation of China (42030308, 42130807, and 42104102).

References

Bendick, R., R. Bilham, J. Freymueller, K. Larson, and G. Yin (2000). Geodetic evidence for a low slip rate in the Altyn Tagh fault system, *Nature* **404,** 69–72, doi: 10.1038/35003555.

Chang, L., and C. Wang (2023). Teleseismic shear wave splitting and intracontinental collision deformation of the northern Tibetan Plateau and the eastern Tarim basin, *Sci. China Earth Sci.* **66,** no. 7, 1556–1568.

Chen, H., S. Yang, Q. Wang, J. Luo, C. Jia, G. Wei, Z. Li, G. He, Y. He, and A. Hu (2006). Sedimentary response to the Early-Mid Permian basaltic magmatism in the Tarim plate, *Geol. China* **33,** no. 3, 545–552.

Chen, X., A. Yin, G. E. Gehrels, E. S. Cowgill, M. Grove, T. M. Harrison, and X. Wang (2003). Two phases of Mesozoic north-south extension in the eastern Altyn Tagh range, northern Tibetan Plateau, *Tectonics* **22,** doi: 10.1029/2001tc001336.

Chen, Y., J.-P. Cogné, and V. Courtillot (1992). New Cretaceous paleomagnetic poles from the Tarim Basin, northwestern China, *Earth Planet. Sci. Lett.* **114,** 17–38.

Chen, Z., H. Gong, and L. Li (2006). Cenozoic uplifting and exhumation process of the Altyn Tagh mountains, *Earth Sci. Front.* **13,** 91.

Cheng, F., Z. Guo, H. S. Jenkins, S. Fu, and X. Cheng (2015). Initial rupture and displacement on the Altyn Tagh fault, northern Tibetan Plateau: Constraints based on residual Mesozoic to Cenozoic strata in the western Qaidam Basin, *Geosphere* **11,** 921–942, doi: 10.1130/ges01070.1.

Christie-Blick, N., and K. T. Biddle (1985). Deformation and basin formation along strike-slip faults, in *Strike-Slip Deformation, Basin Formation, and Sedimentation*, K. T. Biddle and N. Christie-Blick (Editors), Vol. 37, Society of Economic Paleontologists and Mineralogists, 1–34, doi: 10.2110/pec.85.37.0001.

Cui, Q., P. Huangfu, Z.-H. Li, J. Zhao, X. Pei, and Y. Shi (2024). Tarim rotation mechanism and the differential deformation responses along the Tian Shan, *Geophys. J. Int.* **236,** 1275–1287.

de Kool, M., N. Rawlinson, and M. Sambridge (2006). A practical grid-based method for tracking multiple refraction and reflection phases in three-dimensional heterogeneous media, *Geophys. J. Int.* **167,** 253–270.

Deng, Y., W. Levandowski, and T. Kusky (2017). Lithospheric density structure beneath the Tarim basin and surroundings, northwestern China, from the joint inversion of gravity and topography, *Earth Planet. Sci. Lett.* **460,** 244–254.

England, P., and D. McKenzie (1982). A thin viscous sheet model for continental deformation, *Geophys. J. Int.* **70,** 295–321.

Downloaded from http://pubs.geoscienceworld.org/ssa/srl/article-pdf/96/4/2300/7126859/srl-2024314.1.pdf
by University of Cambridge user

Feng, Y., Y. Yu, Y. Chen, X. Liang, and P. Wang (2016). Upper mantle anisotropy analysis around the western Altun Tagh fault, *Chin. J. Geophys.* **59,** 1629–1636, doi: 10.6038/cjg20170620.

Gao, R., P. Li, Q. Li, Y. Guan, D. Shi, X. Kong, and H. Liu (2001). Deep process of the collision and deformation on the northern margin of the Tibetan Plateau: Revelation from investigation of the deep seismic profiles, *Sci. China Earth Sci.* **44,** 71–78, doi: 10.1007/bf02911973.

Guo, Z., Z. Zhang, and J. Wang (1998). Study on the formation and evolution of the Suoerkuli Basin and its relationship with the Altyn fault zone, *Geol. J. Coll. Univ.* **4,** no. 1, 59–63.

He, J., P. Vernant, J. Chéry, W. Wang, S. Lu, W. Ku, W. Xia, and R. Bilham (2013). Nailing down the slip rate of the Altyn Tagh fault, *Geophys. Res. Lett.* **40,** 5382–5386, doi: 10.1002/2013GL057497.

Herquel, G., P. Tapponnier, G. Wittlinger, J. Mei, and S. Danian (1999). Teleseismic shear wave splitting and lithospheric anisotropy beneath and across the Altyn Tagh Fault, *Geophys. Res. Lett.* **26,** 3225–3228, doi: 10.1029/1999GL005387.

Jia, Y., J. Sun, L. Lü, J. Pang, and Y. Wang (2020). Late Oligocene-Miocene intra-continental mountain building of the Harke Mountains, southern Chinese Tian Shan: Evidence from detrital AFT and AHe analysis, *J. Asian Earth Sci.* **191,** 104198.

Jiang, X., Y. Jin, and M. K. McNutt (2004). Lithospheric deformation beneath the Altyn Tagh and West Kunlun faults from recent gravity surveys, *J. Geophys. Res.* **109,** doi: 10.1029/2003JB002444.

Jolivet, M., M. Brunel, D. Seward, Z. Xu, J. Yang, F. Roger, P. Tapponnier, J. Malavieille, N. Arnaud, and C. Wu (2001). Mesozoic and Cenozoic tectonics of the northern edge of the Tibetan plateau: Fission-track constraints, *Tectonophysics* **343,** 111–134.

Kao, H., R. Gao, R.-J. Rau, D. Shi, R.-Y. Chen, Y. Guan, and F. T. Wu (2001). Seismic image of the Tarim basin and its collision with Tibet, *Geology* **29,** 575–578.

Kennett, B. L., E. R. Engdahl, and R. Buland (1995). Constraints on seismic velocities in the Earth from travel times, *Geophys. J. Int.* **122,** 108–124.

Kennett, B. L., M. S. Sambridge, and P. R. Williamson (1988). Subspace methods for large inverse problems with multiple parameter classes, *Geophys. J. Int.* **94,** 237–247.

Li, C., R. D. Van der Hilst, A. S. Meltzer, and E. R. Engdahl (2008). Subduction of the Indian lithosphere beneath the Tibetan Plateau and Burma, *Earth Planet. Sci. Lett.* **274,** 157–168.

Li, H., Y. Shen, Z. Huang, X. Li, M. Gong, D. Shi, and A. Li (2014). The distribution of the mid-to-lower crustal low-velocity zone beneath the northeastern Tibetan Plateau revealed from ambient noise tomography, *J. Geophys. Res.* **119,** no. 3, 1954–1970.

Li, H., J. Yang, and Z. Xu (2006). The constraint of the Altyn Tagh fault system to the growth and rise of the northern Tibetan plateau, *Earth Sci. Front.* **13,** 59.

Li, W., Y. Chen, X. Yuan, W. Xiao, and B. F. Windley (2022). Intracontinental deformation of the Tianshan Orogen in response to India-Asia collision, *Nat. Commun.* **13,** 3738, doi: 10.1038/s41467-022-30795-6.

Li, Y., X. Shan, C. Qu, Y. Liu, and N. Han (2018). Crustal deformation of the Altyn Tagh fault based on GPS, *J. Geophys. Res.* **123,** 10,309–10,322, doi: 10.1029/2018JB015814.

Mann, P., M. R. Hempton, D. C. Bradley, and K. Burke (1983). Development of pull-apart basins, *J. Geol.* **91,** 529–554, doi: 10.1086/628803.

Molnar, P., and P. Tapponnier (1975). Cenozoic tectonics of Asia: Effects of a continental collision: Features of recent continental tectonics in Asia can be interpreted as results of the India-Eurasia collision, *Science* **189,** 419–426, doi: 10.1126/science.189.4201.419.

Molnar, P., B. C. Burchfiel, L. K'uangyi, and Z. Ziyun (1987). Geomorphic evidence for active faulting in the Altyn Tagh and northern Tibet and qualitative estimates of its contribution to the convergence of India and Eurasia, *Geology* **15,** 249–253.

Peltzer, G., P. Tapponnier, and R. Armijo (1989). Magnitude of late quaternary left-lateral displacements along the North Edge of Tibet, *Science* **246,** 1285–1289, doi: 10.1126/science.246.4935.1285.

Rai, S. S., K. Priestley, V. K. Gaur, S. Mitra, M. P. Singh, and M. Searle (2006). Configuration of the Indian Moho beneath the NW Himalaya and Ladakh, *Geophys. Res. Lett.* **33,** doi: 10.1029/2006GL026076.

Rawlinson, N., and M. Sambridge (2004). Wave front evolution in strongly heterogeneous layered media using the fast marching method, *Geophys. J. Int.* **156,** 631–647, doi: 10.1111/j.1365-246X.2004.02153.x.

Rawlinson, N., M. D. Kool, and M. Sambridge (2006). Seismic wavefront tracking in 3D heterogeneous media: Applications with multiple data classes, *Explor. Geophys.* **37,** 322–330, doi: 10.1071/EG06322.

Rawlinson, N., A. M. Reading, and B. L. N. Kennett (2006). Lithospheric structure of Tasmania from a novel form of teleseismic tomography, *J. Geophys. Res.* **111,** doi: 10.1029/2005JB003803.

Schmedes, J., J. B. Roth, R. L. Saltzer, and G. M. Leahy (2012). Imaging the shallow crust using teleseismic tomography, *Bull. Seismol. Soc. Am.* **102,** 1276–1282.

Sethian, J. A. (1996). A fast marching level set method for monotonically advancing fronts, *Proc. Natl. Acad. Sci. Unit. States Am.* **93,** 1591–1595, doi: 10.1073/pnas.93.4.1591.

Shaffer, M., B. R. Hacker, L. Ratschbacher, and A. R. C. Kylander-Clark (2017). Foundering triggered by the collision of India and Asia captured in Xenoliths, *Tectonics* **36,** 1913–1933, doi: 10.1002/2017tc004704.

Shen, F., L. H. Royden, and B. C. Burchfiel (2001). Large-scale crustal deformation of the Tibetan Plateau, *J. Geophys. Res.* **106,** 6793–6816, doi: 10.1029/2000JB900389.

Shen, W., X. Zhu, H. Xie, X. Wang, and Y. He (2022). Tectonic–sedimentary evolution during initiation of the Tarim Basin: Insights from late Neoproterozoic sedimentary records in the NW basin, *Precambrian Res.* **371,** 106598.

Shen, Z., M. Wang, Y. Li, D. D. Jackson, A. Yin, D. Dong, and P. Fang (2001). Crustal deformation along the Altyn Tagh fault system, western China, from GPS, *J. Geophys. Res.* **106,** 30,607–30,621, doi: 10.1029/2001jb000349.

Shi, D., M. Jiang, K. Ma, G. Xue, Y. Dong, G. Poupinet, G. Wittlinger, and G. Herquel (1999). P-wave tomography of the crust and upper mantle structure of the Altyn fault zone, *Chin. J. Geophys.* **42,** no. 3, 341–350.

Shi, D., Q. Yu, G. Poupinet, G. Wittlinger, G. Herquel, and M. Jiang (2007). Receiver function imaging of the crustal structure near the Altyn fault zone and its geodynamic significance, *Acta Geol. Sin.* **1,** 139–148.

Sobel, E. R. (1999). Basin analysis of the Jurassic–Lower Cretaceous southwest Tarim basin, northwest China, *Geol. Soc. Am. Bull.* **111,** 709–724.

Downloaded from http://pubs.geoscienceworld.org/ssa/srl/article-pdf/96/4/2300/7126859/srl-2024314.1.pdf
by University of Cambridge user

Sobel, E. R., N. Arnaud, M. Jolivet, B. D. Ritts, and M. Brunel (2001). Jurassic to Cenozoic exhumation history of the Altyn Tagh range, northwest China, constrained by 40Ar/39Ar and apatite fission track thermochronology, Geological Society of America Memoirs, Vol. 194, 247–267.

Song, X., X. Cheng, X. Lin, and S. Gao (2019). Cenozoic tectonic evolution of the Altyn Tagh: Evidence from sedimentary record in Ruoqiang depression of the southeastern Tarim Basin, *Chin. J. Geol.* **54,** no. 2, 330–344, doi: 10.12017/dzkx.2019.020.

Styron, R., M. Taylor, and K. Okoronkwo (2010). Database of active structures from the Indo-Asian collision, *Eos Trans. AGU* **91,** 181–182, doi: 10.1029/2010eo200001.

Tapponnier, P., Z. Xu, F. Roger, B. Meyer, N. Arnaud, G. Wittlinger, and Y. Jingsui (2001). Oblique stepwise rise and growth of the Tibet Plateau, *Science* **294,** 1671–1677, doi: 10.1126/science.105978.

Tian, F., J. Lei, and X. Xu (2020). Teleseismic P-wave crustal tomography of the Weifang segment on the Tanlu fault zone: A case study based on short-period dense seismic array experiment, *Phys. Earth Planet. In.* **306,** 106521.

VanDecar, J. C., and R. S. Crosson (1990). Determination of teleseismic relative phase arrival times using multi-channel cross-correlation and least squares, *Bull. Seismol. Soc. Am.* **80,** 150–169.

Wallace, K., G. Yin, and R. Bilham (2004). Inescapable slow slip on the Altyn Tagh fault, *Geophys. Res. Lett.* **31,** doi: 10.1029/2004GL019724.

Wang, C. Y., W. D. Mooney, X. Wang, L. Chang, Z. Yao, and H. Lou (2024). Intra-continental collision of the Tarim Basin and the Northern Tibetan Plateau, *J. Geophys. Res.* **129,** no. 7, e2024JB028668, doi: 10.1029/2024JB028668.

Wang, E. (1997). Displacement and timing along the northern strand of the Altyn Tagh fault zone, northern Tibet, *Earth Planet. Sci. Lett.* **150,** 55–64.

Wang, M., and Z. Shen (2020). Present-day crustal deformation of continental china derived from GPS and its tectonic implications, *J. Geophys. Res.* doi; 10.1029/2019jb018774.

Wang, Z., D. Zhao, R. Gao, and Y. Hua (2019). Complex subduction beneath the Tibetan plateau: A slab warping model, *Phys. Earth Planet. In.* **292,** 42–54.

Wittlinger, G., P. Tapponnier, G. Poupinet, J. Mei, S. Danian, G. Herquel, and F. Masson (1998). Tomographic evidence for localized lithospheric shear along the Altyn Tagh Fault, *Science* **282,** 74–76, doi: 10.1126/science.282.5386.74.

Wu, C., T. Xu, X. Tian, R. N. Mitchell, J. Lin, J. Yang, X. Wang, and Z. Lu (2024). Underthrusting of Tarim lower crust beneath the Tibetan Plateau revealed by receiver function imaging, *Geophys. Res. Lett.* **51,** doi: 10.1029/2024gl108220.

Xia, W., N. Zhang, X. Yuan, L. Fan, and B. Zhang (2001). Cenozoic Qaidam basin, China: a stronger tectonic inversed, extensional rifted basin, *AAPG Bull.* **85,** 715–736.

Xie, T., T. Xu, Y. Yang, X. Tian, J. Lin, C. Wu, and Z. Lu (2023). Observation of Higher-Mode Rayleigh waves from ambient noise in the Tarim Basin, China, *Seismol. Res. Lett.* **94,** no. 4, 1848–1859, doi: 10.1785/0220220361.

Xie, T., Y. Yang, T. Xu, X. Tian, J. Lin, C. Wu, and Z. Lu (2024). 2-D sedimentary structures at the southeast margin of the Tarim Basin, China, constrained by Love wave ambient noise tomography, *Geophys. J. Int.* **239,** no. 3, 1775–1788.

Xu, X., Y. Ma, D. Shi, X. Wang, and C. Yin (2009). Application of teleseismic tomography to the study of shallow structure beneath Shizigou in the western Qaidam basin, *Earthq. Sci.* **22,** 189–195.

Xu, X., A. V. Zuza, A. Yin, X. Lin, H. Chen, and S. Yang (2021). Permian plume-strengthened Tarim lithosphere controls the Cenozoic deformation pattern of the Himalayan-Tibetan orogen, *Geology* **49,** 96–100.

Xu, Y., X. Wei, Z. Luo, H. Liu, and J. Cao (2014). The Early Permian Tarim Large Igneous Province: Main characteristics and a plume incubation model, *Lithos* **204,** 20–35, doi: 10.1016/j.lithos.2014.02.015.

Xu, Z., H. Li, Z. Tang, X. Qi, H. Li, and Z. Cai (2011). The transformation of the terrain structures of the Tibet Plateau through large-scale strike-slip faults, *Acta Petrol. Sin.* **27,** no. 11, 3157–3170.

Yao, S., T. Xu, Y. Sang, L. Ye, T. Yang, C. Wu, and M. Zhang (2024). The seismicity in the middle section of the Altyn Tagh Fault system revealed by a dense nodal seismic array, *Earthq. Res. Adv.* **4,** no. 3, 100308, doi: 10.1016/j.eqrea.2024.100308.

Yin, A., and T. M. Harrison (2000). Geologic evolution of the Himalayan-Tibetan Orogen, *Annu. Rev. Earth Planet. Sci.* **28,** 211–280, doi: 10.1146/annurev.earth.28.1.211.

Yin, A., P. E. Rumelhart, R. Butler, E. Cowgill, T. M. Harrison, D. A. Foster, R. V. Ingersoll, Z. Qing, Z. Xian-Qiang, W. Xiao-Feng, *et al.* (2002). Tectonic history of the Altyn Tagh fault system in northern Tibet inferred from Cenozoic sedimentation, *Geol. Soc. Am. Bull.* **114,** 1257–1295.

Zhang, L., M. Unsworth, S. Jin, W. Wei, G. Ye, A. G. Jones, J. Jing, H. Dong, C. Xie, F. Le Pape, *et al.* (2015). Structure of the Central Altyn Tagh Fault revealed by magnetotelluric data: New insights into the structure of the northern margin of the India–Asia collision, *Earth Planet. Sci. Lett.* **415,** 67–79, doi: 10.1016/j.epsl.2015.01.025.

Zhang, P., P. Molnar, and X. Xu (2007). Late Quaternary and present-day rates of slip along the Altyn Tagh Fault, northern margin of the Tibetan Plateau, *Tectonics* **26,** doi: 10.1029/2006tc002014.

Zhao, J., W. D. Mooney, X. Zhang, Z. Li, Z. Jin, and N. Okaya (2006). Crustal structure across the Altyn Tagh Range at the northern margin of the Tibetan plateau and tectonic implications, *Earth Planet. Sci. Lett.* **241,** 804–814, doi: 10.1016/j.epsl.2005.11.003.

Zhao, J., X. Yuan, H. Liu, P. Kumar, S. Pei, R. Kind, Z. Zhang, J. Teng, L. Ding, X. Gao, *et al.* (2010). The boundary between the Indian and Asian tectonic plates below Tibet, *Proc. Natl. Acad. Sci.* **107,** 11,229–11,233, doi: 10.1073/pnas.1001921107.

Zhao, J., P. Zhang, X. Yuan, W. Gan, J. Sun, T. Deng, H. R. Van Der, X. Zhang, H. Liu, X. Yang, *et al.* (2019). Clockwise rotation of the Tarim basin driven by the Indian plate impact, *Earth Sci. Subsoil Use* **42,** no. 4, 425–436.

Zhou, L., L. Zhang, S. Jin, W. Wei, G. Ye, and C. Xie (2023). The crustal electrical structure of a tectono-magmatic rejuvenated craton: Insights from magnetotelluric data of the northwestern Qaidam Basin, northern Tibetan Plateau, *Tectonophysics* **848,** 229719.

Manuscript received 13 August 2024
Published online 27 February 2025

Downloaded from http://pubs.geoscienceworld.org/ssa/srl/article-pdf/96/4/2300/7126859/srl-2024314.1.pdf
by University of Cambridge user